Mobile bioluminescence tomography-guided system for pre-clinical radiotherapy research

Deng, Zijian; Xu, Xiangkun; Iordachita, Iulian; Dehghani, Hamid; Zhang, Bin; Wong, John W.; Wang, Ken Kang-Hsin

DOI:
10.1364/BOE.460737

License:
Other (please specify with Rights Statement)

Document Version
Publisher's PDF, also known as Version of record

Citation for published version (Harvard):
Deng, Z, Xu, X, Iordachita, I, Dehghani, H, Zhang, B, Wong, JW & Wang, KK-H 2022, 'Mobile bioluminescence tomography-guided system for pre-clinical radiotherapy research', *Biomedical Optics Express*, vol. 13, no. 9, pp. 4970-4989. https://doi.org/10.1364/BOE.460737

Research Article | Vol. 13, No. 9 / 1 Sep 2022 / Biomedical Optics Express 4970
Biomedical Optics EXPRESS

Mobile bioluminescence tomography-guided system for pre-clinical radiotherapy research

ZIJIAN DENG,[1,2,6,7] XIANGKUN XU,[1,2,6] IULIAN IORDACHITA,[3] HAMID DEHGHANI,[4] BIN ZHANG,[5] JOHN W. WONG,[1] AND KEN KANG-HSIN WANG[1,2,8]

[1]*Department of Radiation Oncology and Molecular Radiation Sciences, Johns Hopkins University, Baltimore, Maryland 21287, USA*
[2]*Biomedical Imaging and Radiation Technology Laboratory (BIRTLab), Department of Radiation Oncology, University of Texas Southwestern Medical Center, Dallas, Texas 75390, USA*
[3]*Laboratory for Computational Sensing and Robotics, Johns Hopkins University, Baltimore, Maryland 21218, USA*
[4]*School of Computer Science, University of Birmingham, Edgbaston, Birmingham B15 2TT, UK*
[5]*School of Biomedical Engineering, Dalian University of Technology, Dalian, Liaoning 116024, China*
[6]*These authors contributed equally to this work*
[7]*Zijian.Deng@utsouthwestern.edu*
[8]*Kang-Hsin.Wang@utsouthwestern.edu*

Abstract: Due to low imaging contrast, a widely-used cone-beam computed tomography-guided small animal irradiator is less adept at localizing *in vivo* soft tissue targets. Bioluminescence tomography (BLT), which combines a model of light propagation through tissue with an optimization algorithm, can recover a spatially resolved tomographic volume for an internal bioluminescent source. We built a novel mobile BLT system for a small animal irradiator to localize soft tissue targets for radiation guidance. In this study, we elaborate its configuration and features that are indispensable for accurate image guidance. Phantom and *in vivo* validations show the BLT system can localize targets with accuracy within 1 mm. With the optimal choice of threshold and margin for target volume, BLT can provide a distinctive opportunity for investigators to perform conformal biology-guided irradiation to malignancy.

1. Introduction

In radiation therapy (RT), advances in intensity modulation [1,2] and image guidance [3,4] have resulted in highly conformal radiation treatment for clinical use. However, many important radiobiological mechanisms that could facilitate progress in RT have not yet been clarified. Motivated by this, investigators in radiobiology have developed various *in vivo* tumor models for RT research. A major challenge for these investigators is to correctly deliver radiation to the tumors to ensure that their preclinical investigations closely align with clinical practice. Several groups, including ours, have initiated efforts to develop small animal irradiators that mimic clinical RT [5–10]. Identifying a suitable imaging modality for irradiation guidance is crucial for these efforts. Cone-beam computed tomography (CBCT) is a major imaging modality that can provide irradiation guidance for small animal irradiators [11–13], but is less adept at localizing soft tissue targets that grow in a low image contrast environment. Recently, magnetic resonance imaging (MRI) and positron emission tomography (PET) have also been adapted to guide irradiation to tumors *in vivo* [14,15].

Because of its strong imaging contrast, bioluminescence imaging (BLI) offers an appealing solution for soft tissue targeting and has been used extensively in preclinical oncology studies, including assessment of malignancy progression and response to treatment [16–18]. BLI also has unique advantages over the aforementioned imaging modalities. In addition to its compact

#460737 https://doi.org/10.1364/BOE.460737
Journal © 2022 Received 8 Apr 2022; revised 4 Aug 2022; accepted 9 Aug 2022; published 30 Aug 2022

Biomedical Optics EXPRESS

system design and no ionizing radiation involved at low cost, BLI exploits the light that is directly generated from luciferase-targeted living cells with a chemical reaction, and thus provides a background-free image and closely connects signal intensity to cell viability. Furthermore, because many bioluminescent reporter–substrate combinations have been widely applied to visualize molecular and cellular processes, BLI provides a bridge to connect *in vitro* molecular and cellular outcomes, especially malignancy activities, to studies of *in vivo* tumor models [17,19].

The bioluminescent signal, emitted from an internal source, transmits through the tissue, and the surface signal can be detected by an imaging apparatus. However, because optical transport is susceptible to irregular animal torsos and tissue optical properties, BLI is inadequate to infer the internal source distribution for precise irradiation guidance [20]. Recognizing this led us to innovate 3D bioluminescence tomography (BLT) as an image guidance modality for small animal irradiators. In BLT, the surface BLI is measured as input. In tandem with an optimization algorithm, BLT employs a model of light propagation through tissue to the skin surface for reconstruction, which minimizes the deviation between calculated and measured surface bioluminescent data [21,22], to reconstruct the underlying source distribution [23,24].

In this study, we introduce our novel standalone BLT system, designed in mobile mode with a rigid configuration of non-contact imaging geometry that allows distant transportation for various applications. It can be integrated with a small animal irradiator via a transportable mouse bed that allows the imaged animal placed at a natural lying position to be transferred between these two systems. Fiducial markers, which can be identified in both optical and CBCT images, are attached to the bed to register the coordinates of the irradiator and 2D image plane in the BLT system. The standalone design of the BLT system with the transportable bed minimizes the need of modifying existing commercial irradiators and ensures BLI-only applications without occupying the irradiator that affects its experiment throughputs. In our BLT-guided RT workflow, a mouse first undergoes BLI in the BLT system, and later CBCT imaging in small animal irradiator. Based on the registration of system coordinates, surface bioluminescent data are mapped to a numerical mesh established from the CBCT image, followed by BLT reconstruction to retrieve the light source distribution, used as the target volume to guide the irradiator for dose delivery.

We have optimized the design of our BLT system to achieve accurate and quantitative delineation to the target for conformal radiation guidance. A rotatable 3-mirror system combined with optical filters was developed to detect the spectrally-resolved bioluminescent signals from the animal surface at multiple viewing planes, thereby maximizing the data input for tomographic reconstruction [25]. The spectrum and intensity of cell-emitted bioluminescent signals are temperature-sensitive [24]. To maintain a consistent ambient temperature for the imaged animal during BLI session, a thermostatic system was implemented in the imaging system. For the registration of system coordinates, we modeled the assembly of 2D optical image acquisition as a pinhole camera model to precisely map the surface bioluminescent data at any projection angle to the mesh. To eliminate the errors of free-space light propagation from the imaged object surface to the optical detector, we proposed a spectral derivative (SD) algorithm [26] and applied it for this study.

In this work, we first introduce our system and workflow in detail. We then present a study using a mouse phantom implanted with a self-luminous light source to show the source localization capability of our multi-spectral and -projection BLT system. In the last, we demonstrate BLT-guided radiation planning for an *in vivo* orthotopic bioluminescent glioblastoma (GBM) model, based on a planning target volume resolved from a BLT-reconstructed tumor volume. Under a well-defined threshold and radiation margin applied to the reconstructed volume, the uncertainties of the BLT in target localization can be effectively minimized, which lead to high-precision volumetric-guided focal irradiation.

Biomedical Optics EXPRESS

2. Materials and methods

2.1. Configuration of the BLT system

A schematic of the mobile BLT system is shown in Fig. 1(a), and a photo of the actual system, which consists of an optical assembly, a transportable mouse bed, a thermostatic system, and a 1D linear stage (Parker 406XR, B.W.Rogers Co, Morgantown, PA), is shown in Fig. 1(b). The composition of the transportable mouse bed is shown in Fig. 1(c), and Fig. 1(b)-(e) illustrate animal transportation, supported by the bed, between the BLT system and small animal irradiator, i.e. small animal radiation research platform (SARRP; Fig. 1(e)) [5] utilized in our study. The components and layout of the thermostatic system are shown in Fig. 2. Characterization of the imaging system can be found in supplementary material Sec. 1. We describe the technical details of the main modules as follows.

(1) Optical assembly: The optical assembly consists of a charge-coupled device (CCD; 27.6 mm × 27.6 mm back-illuminated sensor at 13.5-μm pixel size, operating at −80 °C; iKon-L 936, Andor Technology, Belfast, UK) and a light-tight enclosure (blue dash box in Fig. 1(a), 1(b)). The front end of enclosure is an imaging chamber (purple dash box in Fig. 1(a), 1(b)), including a rotatable 3-mirror system (silver-coated glass mirrors with 98% reflectivity; H. L. Clausing, Inc., Skokie, IL) with four light emitting diodes (LED; peak at 468 nm; Digi-Key Part Number: 160-1827-1-ND; Lite-On Inc., Milpitas, CA) mounted at its corners (Fig. 1(a1)). The back end of enclosure includes a 50-mm f/1.2 lens (Nikkor, Nikon Inc., Melville, NY) installed at the F-mount CCD, a filter wheel (Edmund Optics Inc., Barrington, NJ), and a home-made rotary stage for motorizing the 3-mirror system. The entire light-tight enclosure was connected to the 1D linear stage via T-slotted aluminum extrusions. For BLI acquisition, the optical assembly is driven by the 1D linear stage to dock onto the mouse bed, and the optical signal emitted from the surface of the imaged object is directed by the 3-mirror system, filtered by selected filter in the filter wheel, and captured by the CCD camera (Fig. 1(a)). The 3-mirror system can rotate in parallel to the camera-lens orientation and 180° around the imaged object for multi-projection imaging (green arrow in Fig. 1(a1)). With the 3-mirror system placed right above the mouse bed, the focal plane was set at ~ 11 mm above the bed's upper surface (see supplementary material Sec. 1). The optical path from the focal plane to the front surface of the lens is 45 cm (red dash line in Fig. 1(a)), and the depth of field (DOF) is 21 mm (see supplementary material Sec. 1). Four 20-nm full width at half maximum (FWHM) band-pass filters (Chroma Technology Corp., Bellows Falls, VT) at 590, 610, 630, and 650 nm were mounted in the filter wheel for multi-spectral imaging. The choice of central wavelength for the band-pass filter is based on the bioluminescent signal spectrum of interest and *in vivo* tissue absorption spectrum. For the *Luc2* + D-luciferin (XenoLight D-Luciferin K+ Salt; PerkinElmer Inc., Waltham, MA) used in this work, the peak of bioluminescent spectrum is at 609 nm and its FWHM is about 100 nm [27]. To minimize the absorption of the bioluminescent signal by tissue medium, the signal spectrum is preferably closer to the tissue near-infrared window. Therefore, the filters at 590, 610, 630, and 650 nm were selected. Because the CBCT of the small animal irradiator is used to generate a tetrahedral mesh of an imaged animal for optical reconstruction and define the coordinate for radiation, the 2D BLIs were mapped onto the animal surface of the CBCT image and used as input data for reconstruction. Eight bearing balls (BBs; polytetrafluoroethylene, 3/32" diameter; McMaster-Carr, Elmhurst, IL; Fig. 1(c)), which can be identified in both optical photo image with the LEDs on and CBCT image, were attached to the bed as fiducial markers for registering the coordinates of the BLT system and irradiator. The LEDs were used to illuminate imaged objects and BBs to identify their positions (Fig. 1(a1)).

Biomedical Optics EXPRESS

(2) Pixel scale of BLI: The pixel scale is the corresponding physical size of CCD pixel at focal plane, which is 0.117 mm per CCD pixel. To balance the image acquisition time and BLT reconstruction accuracy, we used 8×8 binning (0.936 mm/pixel at focal plane) for BLI acquisition. The rule of thumb is to keep the pixel scale close to 1 mm, about the order of reduced scattering length of photon in tissue. A pixel scale smaller than 1 mm is unlikely to significantly improve reconstruction accuracy.

(3) Transportable mouse bed: The transportable mouse bed (Fig. 1(c)) is used for holding an imaged object in the BLT system and irradiator, as well as supporting the object transport between these two systems (Fig. 1(b-e)). The bed consists of a bed base, a nose cone, two anesthesia hoses (inner diameter: 3.2 mm, outer diameter: 6.4 mm; U.S. Plastic Corp., Lima, OH), and eight BBs. The bed base and nose cone were painted in black to eliminate light reflection to the CCD. To comfort the imaged mouse during experiment and adapt to commercial irradiators, the bed base supports the animal in any natural position. The two anesthesia hoses are connected to the nose cone, and one of the hoses is linked to an anesthesia machine (Fig. 1(d)), allowing the animal to be anesthetized during imaging, transportation, and irradiation. For surface BLI acquisition, the bed is connected to the mouse bed support (Fig. 1(b)) in the BLT system, and the optical assembly is driven by the motorized linear stage to dock onto the bed. The center of the bed is designed close to the center of the image field of view. After the BLI session, the bed carrying the anesthetized animal is detached from the BLT system, and transferred to the irradiator for CBCT imaging, followed by BLT-guided irradiation. The BLT system is operated in proximity (within 2 m) to the irradiator to minimize the uncertainty caused by animal transportation [28].

(4) Thermostatic system: The thermostatic system, built in light-tight enclosure (except heat gun), comprises two modules for boosting and maintaining the temperature around the imaged object at 37 °C, respectively. A heat gun and a heat transport pipeline, attached on top of the light-tight enclosure, compose the temperature-boosting module (Fig. 2(a)). The outlet of the heat gun is linked to two openings at the front of the imaging chamber via the heat transport pipeline. The temperature maintenance module consists of a resistor, a thermocouple with monitor (both acquired from an egg incubator; Brower Equipment, Houghton, IA), and seven fans (Digi-Key Part Number: 102-4362-ND; CUI Inc., Tualatin, OR) (Fig. 2(b)). The resistor was positioned at bottom edges of the side wall and all the edges at the front face except its bottom edge (black line around inner wall of imaging chamber in Fig. 2(b)). The thermocouple is fixed under the 3rd mirror of the 3-mirror system to closely measure the temperature around imaged object. Four fans were placed at the front corners, two at each corner, and three fans were placed on the front-top end of the chamber to circulate the heat generated from the resistor to maintain temperature uniformity throughout the chamber. Before BLI acquisition, we used the heat gun to boost the chamber temperature to 37 °C, and relied on the resistor to maintain the temperature during imaging course.

Because the thermocouple is positioned at the 3-mirror system, ~ 5 cm away from the center of mouse bed base, we further confirmed the validity of using the thermocouple reading as the surrogate to estimate the temperature around the bed. We placed a thermometer on the bed base to record the actual temperature of its periphery. Figure 2(c) shows that under the heat circulation by the seven fans, our system thermocouple can accurately demonstrate the temperature around the bed during the entire routine of heating control within 40 minutes.

Biomedical Optics EXPRESS

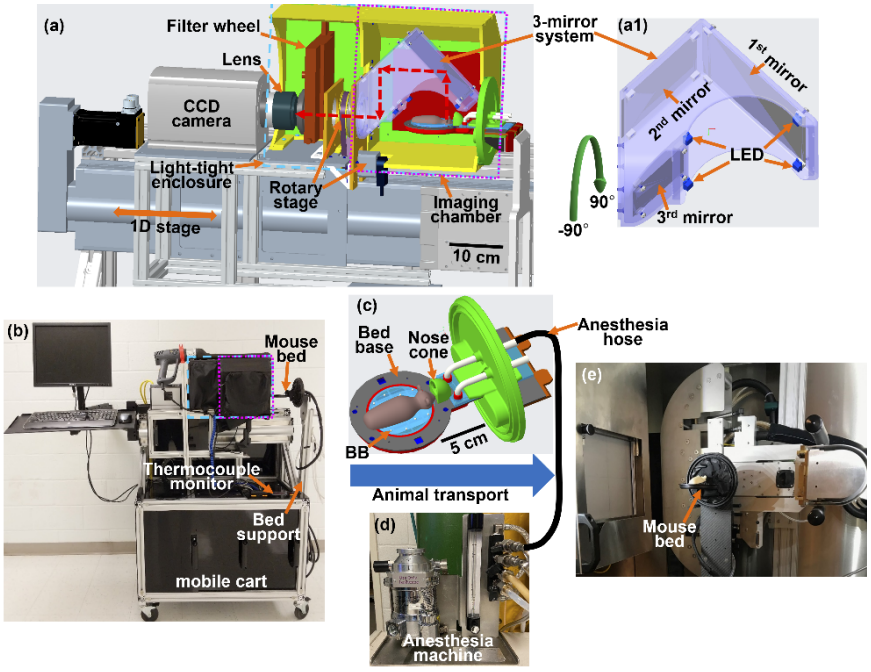

Fig. 1. BLT system in standalone and mobile design; (a) schematic of the BLT system, including optical assembly, mouse bed, and 1D linear stage, and (a1) zoom-in view of 3-mirror system showing positions of mirrors and LEDs; the blue dash box indicates the light-tight enclosure, and the purple dash box shows the imaging chamber as the front part of the light-tight enclosure. The optical assembly can be docked to the mouse bed driven by the 1D linear stage. The red dash line indicates the optical path from the imaging plane through the 3-mirror system and selected filter to the front surface of the lens. After optical image acquisition, the imaged animal is detached from (b) the BLT system along with (c) a transportable mouse bed under (d) anesthesia of isoflurane, and transferred to (e) a small animal irradiator for CBCT imaging and BLT reconstruction for BLT-guided irradiation.

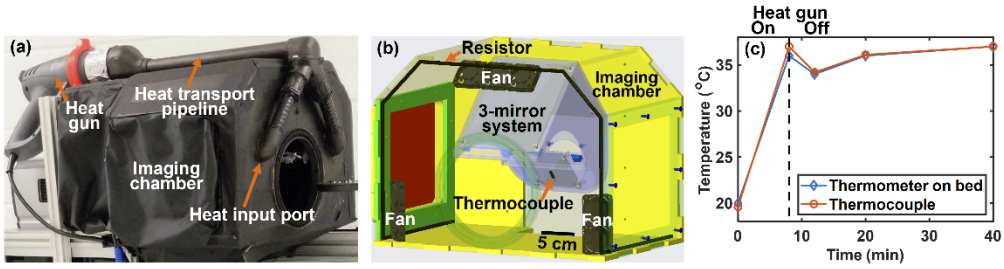

Fig. 2. Design of thermostatic system; (a) photo of partial BLT system showing components of the thermostatic system outside the light-tight enclosure; (b) schematic of the imaging chamber interior, depicting the layout of thermostatic system inside the chamber; (c) temperature measurement by a thermometer positioned on mouse bed and the thermocouple of thermostatic system.

Biomedical Optics EXPRESS

2.2. Bioluminescence image acquisition

System-specific source spectrum was measured before BLI for imaged object to improve the accuracy of multi-spectral approach [24]. A self-luminous light source (glass capillary at 9.8 mm × 2.8 mm × 1.5 mm, internally coated with zinc sulfide and filled with tritium gas; Trigalight, mb-microtec ag, Niederwangen, Switzerland) and an orthotopic GBM (grown from GL261-*Luc2* cells), used as light sources for imaged objects, mouse phantom and *in vivo* GBM mouse model, respectively, were quantified for the system-specific source spectra via BLI session (see supplementary material Sec. 2). The spectrum weights of the GL261-*Luc2* at 590, 610, 630, and 650 nm are 0.8037 ± 0.0025, 1, 0.8423 ± 0.0006, and 0.4931 ± 0.0001 (n = 4 petri dishes), respectively. The spectrum weights of the self-luminous light source are 0.942, 1, 0.895, and 0.650 at 590, 610, 630 and 650 nm, respectively. These spectra were used to correct multi-spectral surface BLI data.

After the measurement of source spectrum, the imaged objects underwent multi-projection at −90°, 0°, and 90° and multi-spectral at 590, 610, 630, and 650 nm BLI acquisition. In preparation of GBM-bearing mouse for the BLI session, mouse hair was shaved with a clipper, followed by depilation with hair removal lotion. The interior of the imaging chamber was warmed up and maintained at 37 °C before the BLI course. BLI was conducted 10 minutes after intraperitoneal injection of D-Luciferin (125 µl, 30 mg/ml for 25 g mouse to reach 150 mg/kg). The GBM-bearing mouse was immobilized on the mouse bed at prone position and anesthetized with 1–2% isoflurane (Fluriso, MWI Veterinary Supply Co. Boise, ID) in oxygen during imaging. BLIs were acquired at 8 × 8 binning, 4× pre-amplifier gain, and 1 MHz readout rate. Since the *in vivo* bioluminescence signal can vary over time and the signal variation is animal-specific, open field (without filter) images were acquired before and after each spectral image to establish a time-resolved curve for recording signal variation over time (see supplementary material Sec. 3) [24]. This time-resolved curve was used to correct the intensity of each spectral image taken at certain time point. The detected *in vivo* BL signal at 590 nm was much lower than that at other 3 wavelengths, and the large ratio of BL signals between 610 and 590 nm could introduce numerical errors for our SD-based reconstruction. Therefore, for the study of *in vivo* GBM-bearing mouse, we chose the images at 610, 630, and 650 nm for BLT reconstruction.

After acquiring BLI, photo images at −90°, −45°, 0°, 45°, and 90° projections were taken for the BB positions on the mouse bed to retrieve geometrical parameters (see Sec. 2.4), which are used for mapping the BLI onto a 3D mesh surface generated from the CBCT image.

2.3. CBCT imaging

After BLI, the animal along with the mouse bed was transferred from the optical system to SARRP [5] for CBCT imaging. SARRP consists of a dual focal X-ray source mounted on a 360° rotational gantry, an amorphous silicon flat panel detector and a 4D (3-axis translation and 360° rotation) robotic base. For SARRP CBCT imaging, the X-ray source employed a 0.4 mm focal spot at 65 kVp and 0.7 mA with 1 mm thick aluminum filter. A CBCT image was acquired by rotating the animal with the 4D robotic base between the X-ray source and detector panel. The animal was anesthetized with 1-2% isoflurane in oxygen during the transportation and imaging course. The acquired SARRP CBCT image was used to: 1) provide animal surface to generate a tetrahedral mesh for the finite element method (FEM)-based BLT reconstruction, and 2) define a 3D coordinate in SARRP for radiation planning and focal irradiation.

Contrast CBCT was used to assess the *in vivo* GBM volume and location to validate BLT reconstruction [29]. It is worthwhile to mention that for day-to-day biology experiment, the contrast image is not ideal for image-guidance using small animal irradiator, limited by fast contrast clearance and CBCT performance of commercial irradiator. The center of mass (CoM) of the contrast-labelled GBM volume was calculated to assess BLT localization accuracy. After the SARRP CBCT imaging session, the mouse was moved to our in-house high resolution CBCT

Biomedical Optics EXPRESS

system [30] for contrast CBCT imaging. The mouse was imaged 1 minute after retro-orbital injection of the contrast reagent at a dose of 2 gI/kg (Iodixanol, 320 mgI/ml; Visipaque, GE Health Care, Chicago, IL).

2.4. Data mapping for multi-projection BLIs

SARRP CBCT image defines the coordinate used for BLT reconstruction. Therefore, we proposed a geometry calibration method modified from Cao *et al* [31] to map the 2D BLI acquired at a given projection angle onto the mesh surface generated from the CBCT image. The mapped BLIs were used as input data for BLT reconstruction. Briefly, our approach includes two steps: 1) registering 3D CBCT coordinate to 3D optical coordinate with rigid transformations, and 2) projecting the 3D optical coordinate to 2D optical coordinate at CCD image plane that is the CCD sensor array. Once the 3D CBCT and 2D optical coordinates are registered, the 2D BLI acquired at any projection can be mapped onto the mesh surface.

The orientations of 3D CBCT (O_s-$X_sY_sZ_s$), 3D optical (O-XYZ), and 2D optical (o-$\mu\nu$) coordinates are defined in Fig. 3. For the 3D optical coordinate, the Y axis is defined at the rotational axis of the 3-mirror system and toward the CCD. The rotated 3D optical coordinate is defined as O-$X'Y'Z'$. For the rotation around the Y axis, the position where the 3-mirror system is right above the mouse bed is labelled as 0°, the clockwise rotation is defined as positive direction, and the range of rotation is defined from −90° to 90°. We note that the mechanical rotation of the mirror is defined reversely relative to the 3D optical coordinate around the Y axis. The virtual image plane, defined as a reflection-free plane equivalent to that at actual CCD sensor array after multiple reflections through the 3-mirror system, is perpendicular to Z axis or Z' axis after rotation. The 2D optical coordinate is located at the virtual image plane, and its axes, μ and ν, are parallel to the X and Y axes, respectively.

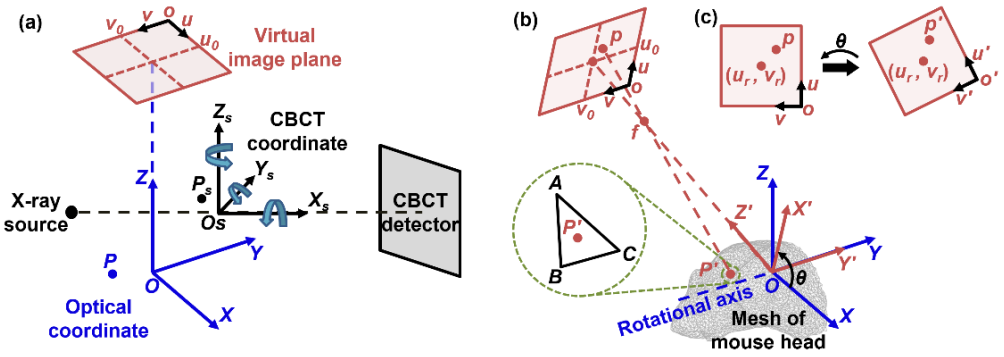

Fig. 3. Mechanism of 2D BLI mapped to mesh surface from 3D CBCT image; (a) translational and rotational shifts transform the 3D CBCT coordinate to 3D optical coordinate. (b) A pinhole camera model is used to project the rotated 3D optical coordinate to the 2D virtual image plane. (c) The 2D optical coordinate of virtual image plane is rotated to match the acquired image, which is rotated due to the combination of the stationary CCD and motorized 3-mirror system.

The registration between the 3D CBCT and 2D optical coordinates requires knowledge about the following 12 geometrical parameters (Fig. 3).

1) X_{Ot}, Y_{Ot}, Z_{Ot}, translational shifts between 3D CBCT and 3D optical coordinates.

2) θ_{Xs}, θ_{Ys}, θ_{Zs}, rotational shifts between 3D CBCT and 3D optical coordinates.

3) L_{fd}, distance from the focal point, f, to the 2D optical image plane.

Biomedical Optics EXPRESS

4) L_{fo}, distance from the focal point, f, to the 3D optical coordinate origin O.

5) μ_0, ν_0, center of the 2D optical image.

6) μ_r, ν_r, rotation center of 2D optical image; due to the 3-mirror rotation with the static CCD camera, the 2D images were rotated accordingly during multi-projection imaging.

Rigid transformations, including translational and rotational shifts, were applied for registering the 3D CBCT coordinate to the 3D optical coordinate (Fig. 3(a)). For a given point in the 3D CBCT space P_s, its position in the 3D CBCT P_s (X_s, Y_s, Z_s) and 3D optical P (X, Y, Z) coordinates is linked by ($P_s \rightarrow P$)

$$\begin{bmatrix} X \\ Y \\ Z \end{bmatrix} = R_{Xs}(\theta_{Xs}) \cdot R_{Ys}(\theta_{Ys}) \cdot R_{Zs}(\theta_{Zs}) \cdot \begin{bmatrix} X_s + X_{Ot} \\ Y_s + Y_{Ot} \\ Z_s + Z_{Ot} \end{bmatrix}, \tag{1}$$

where,

$$R_{Xs}(\theta_{Xs}) = \begin{bmatrix} 1 & 0 & 0 \\ 0 & \cos(\theta_{Xs}) & -\sin(\theta_{Xs}) \\ 0 & \sin(\theta_{Xs}) & \cos(\theta_{Xs}) \end{bmatrix}, \tag{2}$$

$$R_{Ys}(\theta_{Ys}) = \begin{bmatrix} \cos(\theta_{Ys}) & 0 & \sin(\theta_{Ys}) \\ 0 & 1 & 0 \\ -\sin(\theta_{Ys}) & 0 & \cos(\theta_{Ys}) \end{bmatrix}, \tag{3}$$

$$R_{Zs}(\theta_{Zs}) = \begin{bmatrix} \cos(\theta_{Zs}) & -\sin(\theta_{Zs}) & 0 \\ \sin(\theta_{Zs}) & \cos(\theta_{Zs}) & 0 \\ 0 & 0 & 1 \end{bmatrix}. \tag{4}$$

$R_{Xs}(\theta_{Xs})$, $R_{Ys}(\theta_{Ys})$ and $R_{Zs}(\theta_{Zs})$ are 3D rotation matrices with the rotation angles θ_{Xs}, θ_{Ys}, and θ_{Zs}, around X_s, Y_s and Z_s axes, respectively.

To project the 3D optical coordinate to the 2D optical coordinate at the virtual image plane, we modeled our CCD camera as an ideal pinhole camera. The projection geometry from the 3D optical coordinate after the mirror rotated at θ degree around Y axis to the 2D optical coordinate in pinhole camera modeling is shown in Fig. 3(b). No shift between Y and Y' axes was considered in this work. For the given point in the 3D optical space P, its position between the coordinates before P (X, Y, Z) and after P' (X', Y', Z') rotation can be expressed as ($P \rightarrow P'$)

$$\begin{cases} X' = X \cdot \cos\theta + Z \cdot \sin\theta \\ Y' = Y \\ Z' = -X \cdot \sin\theta + Z \cdot \cos\theta \end{cases}. \tag{5}$$

With the pinhole camera modeling and Eq. (5), the given point in the rotated 3D optical space P' (X', Y', Z') projected to the virtual image plane p (μ, ν) can be expressed as ($P' \rightarrow p$)

$$\mu = \mu_0 + \frac{L_{fd} \cdot X'}{F \cdot (L_{fo} - Z')} = \mu_0 + \frac{L_{fd} \cdot (X \cdot \cos\theta + Z \cdot \sin\theta)}{F \cdot (L_{fo} + X \cdot \sin\theta - Z \cdot \cos\theta)}, \tag{6}$$

Biomedical Optics EXPRESS

$$\nu = \nu_0 - \frac{L_{fd} \cdot Y'}{F \cdot (L_{fo} - Z')} = \nu_0 - \frac{L_{fd} \cdot Y}{F \cdot (L_{fo} + X \cdot \sin\theta - Z \cdot \cos\theta)}, \tag{7}$$

where F is physical pixel size of our CCD sensor array at 13.5 μm/pixel.

In our BLT system, the CCD camera is kept stationary while the 3-mirror system is rotated for acquiring multi-projection images. Under this optical geometry, if the image is acquired after the 3-mirror system is rotated θ degree, the image projected at CCD chip will be rotated θ degree around the image rotation center (μ_r, ν_r). Therefore, the projected point at the 2D optical coordinate of virtual image plane p (μ, ν) needs to be rotated θ degree around (μ_r, ν_r) to match the acquired image (Fig. 3(c)), which becomes p' (μ', ν') and can be expressed as ($p \rightarrow p$')

$$\begin{bmatrix} \mu' \\ \nu' \end{bmatrix} = \begin{bmatrix} \cos\theta & -\sin\theta \\ \sin\theta & \cos\theta \end{bmatrix} \times \begin{bmatrix} \mu - \mu_r \\ \nu - \nu_r \end{bmatrix} + \begin{bmatrix} \mu_r \\ \nu_r \end{bmatrix}. \tag{8}$$

From Eqs. (1–8), we can register the object surface points on the 3D CBCT volume to the 2D optical image. Therefore, the measured optical signal at a given pixel can be mapped on the mesh surface. To retrieve the 12 geometrical parameters listed in 1)-6) and employed in Eqs. (1–8), we used the eight BBs on the mouse bed as fiducials that can be seen in optical photography images at -90°, -45°, 0°, 45°, and 90° projection and CBCT image. An optimization program with a constrained multivariable optimization function (fmincon; MATLAB R2019b, The MathWork Inc., Natick, MA) was developed to retrieve the geometrical parameters by minimizing the deviation between the calculated p' (μ', ν') and measured BB positions in the 2D optical coordinate. In this optimization routine, the BB positions in the optical photos are used as the measured positions, and the corresponding BB positions retrieved from the geometrical parameters that are under optimization and the markers positions in CBCT image based on Eqs. (1–8) are used as the calculated positions. After the 2D optical and 3D CBCT coordinate is registered, for a point of interest on the mesh surface in 3D CBCT coordinate, we can retrieve its corresponding position and BL reading on the CCD image plane, and linked it to the centers of mesh surface triangle, i.e. P' in Fig. 3(b). This geometric calibration is performed for each imaging session to ensure accurate data mapping for BLT reconstruction.

To validate the accuracy of the data mapping method, 11 BBs were placed on a mouse phantom (XFM-2, Perkin Elmer Inc., Waltham, MA) and imaged at −90°, 0°, and 90° projections, commonly used for our multi-projection BLIs, with the LEDs on. The measured positions of the 11 BBs on these optical photos were used to verify the corresponding BB positions calculated from the data mapping method (see Sec. 3.1).

We further provide the detail of our data selection protocol. For the overlapped region between two projections, the maximum value at a given surface point among the projections is chosen as the data value. The mapped surface data points with values larger than 10% of the maximum value among all the surface points are used as the final input data for reconstruction.

2.5. Mathematical framework for BLT reconstruction

Because light transport in tissue is dominated by scattering, the diffusion approximation (DA) to the radiative transfer equation was applied in our work to model light propagation in tissue media [32]. In continuous wave mode, the DA with the Robin-type boundary condition is expressed as

$$\begin{cases} -\nabla \cdot D(r)\nabla\Phi(r) + \mu_a(r)\Phi(r) = S(r), r \in \Omega \\ \Phi(\xi) + 2A\hat{n} \cdot D(\xi)\nabla\Phi(\xi) = 0, \xi \in \partial\Omega \end{cases}, \tag{9}$$

where $\Phi(r)$ is the photon fluence rate at location r in domain Ω, $D(r) = 1/[3(\mu_a + \mu_s')]$ is the diffusion coefficient, and μ_a and μ_s' are absorption and reduced scattering coefficients, respectively,

Biomedical Optics EXPRESS

at a given wavelength λ. $S(r)$ is the bioluminescence source distribution. ξ represents points on the tissue boundary, and coefficient A can be derived from Fresnel's law, depending on the refractive index of tissue and air. $\hat{\boldsymbol{n}}$ is the unit vector pointing outward, normal to the boundary $\partial\Omega$. Equation (9) can be further expressed in the form of a systematic linear equation as

$$G_\lambda w_\lambda S = \varphi_\lambda, \tag{10}$$

where G_λ is the sensitivity matrix describing the changes of surface fluence rate φ_λ related to source S for a given wavelength λ, which can be constructed from prior knowledge of the optical properties of imaged object, and w_λ is the system-specific light source spectrum.

In the non-contact imaging geometry, as shown in Fig. 1(a), a major challenge is accounting for light propagation from subject surface to the optical detector (CCD camera in our system). Instead of directly using surface BLIs acquired at different wavelengths (φ_{590}, φ_{610}, φ_{630}, φ_{650}), we mapped the ratio images at adjacent wavelengths ($\varphi_{610}/\varphi_{590}$, $\varphi_{630}/\varphi_{610}$, $\varphi_{650}/\varphi_{630}$), which is called the SD data [26], as the input for BLT reconstruction. Our assumption is the BLIs at adjacent wavelengths encountering a near-identical system response, i.e. light emitted from a surface point at the adjacent wavelengths passing approximately same optical path toward the detector. By using the ratio of the BLI data, we can eliminate the geometric dependence of the free spacing light propagation, and therefore, the need for complicated system modeling.

In the non-contact imaging geometry, the surface fluence rate can be rewritten as $\varphi_\lambda = b_\lambda n$, where n is an angular dependent factor, assumed to be spectrally invariant, to account for the difference between actual surface fluence rate and BLI measurement b_λ. Equation (10) becomes

$$G_\lambda w_\lambda S = b_\lambda n. \tag{11}$$

By applying a logarithm to Eq. (11) and considering the ratio of the data between two neighboring wavelengths λ_i and λ_{i+1}, we can write the SD form of Eq. (11) as

$$\left[\frac{\log b_{\lambda_i} n}{b_{\lambda_i} n} G_{\lambda_i} w_{\lambda_i} - \frac{\log b_{\lambda_{i+1}} n}{b_{\lambda_{i+1}} n} G_{\lambda_{i+1}} w_{\lambda_{i+1}}\right] S = \log \frac{b_{\lambda_i}}{b_{\lambda_{i+1}}}. \tag{12}$$

The G_λ is generated by a modified version of our MATLAB (R2019b)-NIRFAST [33] package. The source distribution S in the SD form (Eq. (12)) is iteratively solved by applying a compressive sensing conjugate gradient (CSCG) optimization algorithm [34]. The values of μ_a 0.035, 0.010, 0.005 and 0.004 mm^{-1}, and μ_s' 1.75, 1.66, 1.58 and 1.50 mm^{-1} for 590, 610, 630, and 650 nm, respectively, provided by Perkin Elmer, were used for the BLT reconstruction for mouse phantom, as the phantom was made by spectral-dependent but homogeneous tissue-mimic material. The values of μ_a 0.161, 0.082 and 0.058 mm^{-1}, and μ_s' 1.56, 1.51, and 1.46 mm^{-1} of mouse brain for 610, 630, and 650 nm, respectively [35], were used for the *in vivo* GBM BLT reconstruction.

2.6. Threshold for BLT-reconstructed volume and margin determination for irradiation guidance

The volume of reconstructed source distribution can depend on the choice of the threshold value. For the *in vivo* GBM model, we assessed the optimal threshold using Dice coefficient between the gross target volume (GTV) delineated by contrast CBCT, taken as ground truth, and the tumor distribution reconstructed by our BLT approach (GTV_{BLT}), as $2(GTV_{BLT} \cap GTV)/(GTV_{BLT} + GTV)$ [24]. Furthermore, a uniform margin that accounts for the uncertainties of BLT target localization, including positioning and volume delineation, was added to GTV_{BLT} to form a planning target volume (PTV_{BLT}) for radiation guidance. The margin size is determined by achieving full coverage to GTV and reducing normal tissue radiation toxicity. The coverage to GTV is defined as $(PTV_{BLT} \cap GTV)/GTV$. The coverage to normal tissue is defined as $(PTV_{BLT} - PTV_{BLT} \cap GTV)/V_{head}$, where V_{head} is the volume of mouse

Biomedical Optics EXPRESS

head. To add the margin onto the GTV_{BLT}, we imported the GTV_{BLT} from the MATLAB to 3D Slicer (version 4.10.2) [36,37] and used the function "Margin" in module "Segment Editor" of the 3D Slicer to expand the GTV_{BLT} to form the PTV_{BLT}. By using the treatment planning system (TPS) of SARRP, MuriPlan (Xstrahl Inc., Suwanee, GA), we designed one simple and one complex BLT-guided radiation plans, which, respectively, deploy 2 static beams and 12 hybrid (static + arc) beams, for the *in vivo* orthotopic GBM, guided by the PTV_{BLT}. The dosimetric goal for tumor coverage was 5 Gy prescribed dose covering 95% of the PTV_{BLT}. For each treatment plan, conformity index was assessed to quantify the conformity level of dosage to PTV_{BLT}, and it is defined as V_{RI}/PTV_{BLT}, where V_{RI} is the distribution of reference isodose [38].

2.7. Workflow of BLT-guided RT

For the sake of reader's convenience, the workflow of applying our BLT system with CBCT-equipped small animal irradiator for BLT-guided RT is summarized in Fig. 4.

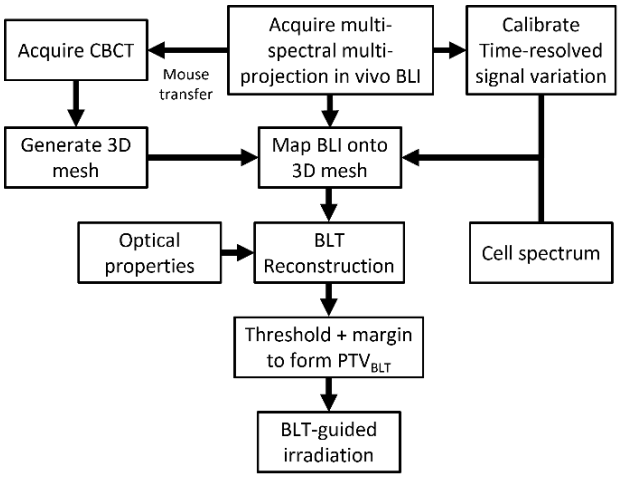

Fig. 4. Workflow of BLT-guided irradiation using our BLT system with a CBCT-equipped small animal irradiator.

3. Results

3.1. Validation of data mapping

The accuracy of mapping 2D BLIs to the mesh surface generated from 3D CBCT is demonstrated in Fig. 5. The 8 BBs glued on the mouse bed, used as fiducials to retrieve the 12 geometrical parameters of the optical system (see Sec. 2.4), are indicated in Fig. 5(a) (orange boxes). To assess the accuracy of the data mapping, we taped 11 BBs on the mouse phantom. The positions of these 11 BBs were directly measured from the 2D optical images taken at −90°, 0°, and 90° projections, and were compared to the corresponding positions calculated by our calibration routine (Fig. 5(b)). The average and standard deviation between the measured and calculated positions of the plastic balls is 0.26 ± 0.03mm for 6 repeated experiments. The maximum deviation is 0.56 mm over all the BBs among all experiments. This result indicates that we can register 2D optical to the 3D CBCT coordinate at sub millimeter accuracy.

3.2. Phantom study for multi-spectral and -projection BLT

A mouse phantom with an implanted self-luminous light source was used to illustrate the target localization of our multi-spectral and -projection BLT system. Figure 6(a) shows the BLIs taken

Biomedical Optics EXPRESS

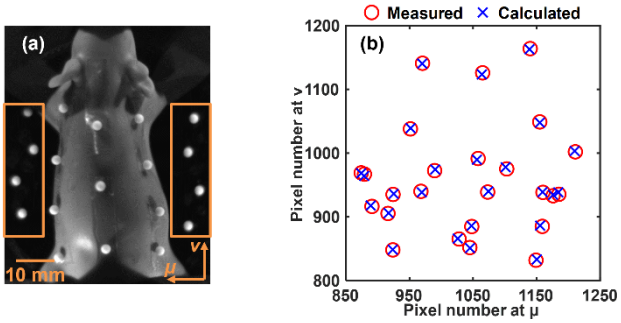

Fig. 5. (a) The 8 BBs taped on the mouse bed, within orange boxes, were used as fiducial markers to retrieve geometric parameters for data mapping, and the balls taped on the mouse phantom were used to assess the accuracy of the mapping. (b) Validation of data mapping; red circles represent the location, directly measured from 2D optical images, of the BBs glued on the mouse phantom (see a), and the blue crosses represent the corresponding locations calculated from our calibration routine.

at −90°, 0°, and 90° projections, then mapped to the mesh surface generated from the phantom CBCT image for BLT reconstruction (Fig. 6(b1)). To investigate the impact of multi-spectral bioluminescent data to the reconstruction accuracy, we compared the reconstruction results of 4 wavelengths (590, 610, 630, 650 nm, Fig. 6(b2-b4)) vs. 3 wavelengths (610, 630, 650 nm, Fig. 6(b5-b7)). The rationale we varied the data at 590 nm is that the bioluminescence is mostly attenuated at 590 nm in phantom and *in vivo* tissue within the chosen range of 590-650 nm. The BLT-reconstructed volume of the 4-wavelength case is qualitatively matched to the actual source (rectangular shape shown in the CBCT images), with CoMs deviation, i.e. localization accuracy, of 0.63 mm (Fig. 6(b2-4)). In contrast, the reconstructed volume of the 3-wavelength case was recovered with the CoM 3.97 mm away from that of actual source (Fig. 6(b5-7)), showing inferior localization accuracy.

To demonstrate the need of multi-projection images, BLIs projected at 0° (Fig. 6(c1)) and 90° (Fig. 6(d1)) were respectively mapped on the mesh surface for reconstruction. BLI data at all 4 wavelengths were used in both cases. Because of the implanted light source's position, the BLI at 0° projection (Fig. 6(c1)) included most of the surface signals shown in the 3-projection case (Fig. 6(b1)). The resulted BLT-reconstructed volume is therefore similar to that from the 3-projection data with slightly worse localization accuracy (Fig. 6(c2-4) with CoM deviation 0.91 mm vs. Figure 6(b2-4) with CoM deviation 0.63 mm). However, the BLI at 90° projection (Fig. 6(d1)) missed some key features of the surface pattern, which introduced deficient information for BLT reconstruction, and thus deviated the recovered volume from the ground truth with 2.64 mm CoMs offset (Fig. 6(d2-4)).

3.3. *In vivo* target localization

We employed an orthotopic GBM-bearing mouse model (18-day-old tumor initiated with 1.2×10^5 GL261-*Luc*2 cells) to illustrate how to use the BLT system to delineate *in vivo* target for radiation guidance. The detail of the establishment of orthotopic GBM model can be found in supplementary material Sec. 4. The BLIs taken at −90°, 0°, and 90° projections are shown in Fig. 7(a). The time-resolved *in vivo* bioluminescence plot (Fig. 7(b)), established from the open-field BLI at −90°, 0°, and 90° projections, shows the variation of the bioluminescent signal over the entire multi-projection and -spectral imaging course. The BLIs corrected by the system-specific source spectrum and time-resolved *in vivo* signal variation were mapped to the

Biomedical Optics EXPRESS

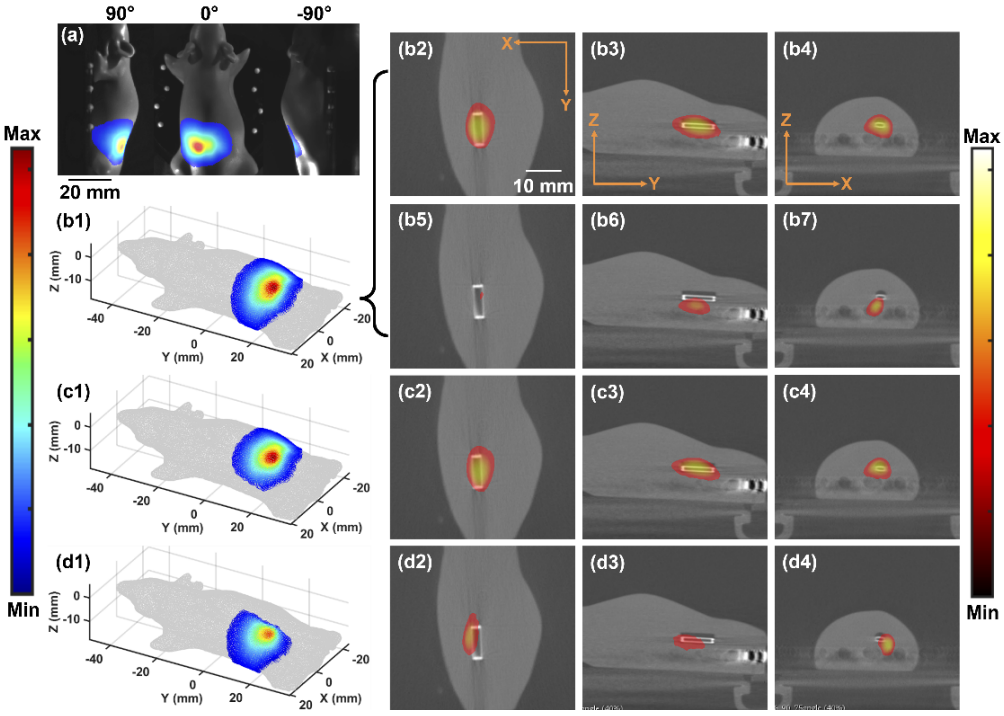

Fig. 6. Data mapping and BLT reconstruction of a phantom with an implanted self-luminated light source; (a) 630-nm BLIs taken at −90°, 0°, and 90° projections; the BLIs were mapped onto the mesh surface after the source spectrum was corrected. (b1) Image of the mapped 3-projection BLIs at 630 nm; to validate the impact of multi-spectral inputs to the reconstruction accuracy, BLT reconstructions were performed (b2-4) with and (b5-7) without the data at 590 nm. Two scenarios of single-projection data mapping were used to show the importance of multiple projections to the reconstruction accuracy. Images of mapped (c1) 0°- and (d1) 90°-projection BLIs at 630 nm, and their corresponding BLT reconstruction results (c2-4, d2-4) are shown. Data > 10% of the maximum of BLI values are displayed in (a), (b1), (c1), and (d1).

mesh surface generated from the mouse CBCT image (Fig. 7(c)). For the threshold of delineating BLT-reconstructed volume, we used Dice coefficient to determine an optimal value (within 0.1–0.8, at 0.1 interval) that provides the most overlapped volume between the GTV_{BLT} and GTV [24]. For this study, 0.4 of maximum of GTV_{BLT} values as the threshold provided the highest Dice coefficient, which is 0.75. Moreover, with the 0.4 threshold, the GTV_{BLT} is overlapped with the GTV at 0.36 mm CoM deviation. For imaging-guided irradiation, the uncertainties of target localization and volume delineation are necessary to be accounted for effective radiation coverage. One solution is to add treatment margin to target. Without margin, inferior tumor coverage by GTV_{BLT} (82.2%) is observed. By adding a uniform 0.75-mm margin on the GTV_{BLT} to form PTV_{BLT}, the PTV_{BLT} can significantly increase the GTV coverage at 100% level with 1.8% normal tissue inclusion. Figure 7(d1-3) provide the visualization for the cases of GTV_{BLT} derived from the 0.4 threshold and 0.75-mm margin expansion, and how this combination is in relative to the coverage to tumor, i.e. GTV.

Biomedical Optics EXPRESS

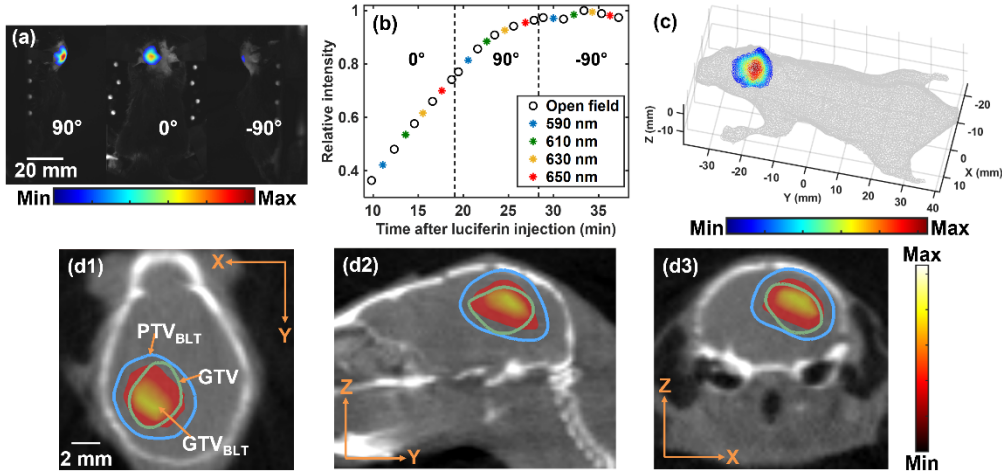

Fig. 7. Data mapping, BLT reconstruction, and margin design for a mouse bearing 18-day-old GBM; (a) 630-nm BLIs taken at 3 projections; (b) formation of overall dynamic change of bioluminescence signal established from open field images at 3 projections; variations of spectral image intensity were interpolated from this time-resolved signal record. (c) image of 3-projection BLIs at 630 nm mapped onto the mesh surface after correcting time-resolved signal variations and source spectrum; data > 10% of the maximum among the 3 projections are displayed in (a) and (c). (d1-3) Three views of CBCT image overlapped with GTV (green contour), GTV_{BLT} (heat map), and PTV_{BLT} (blue contour) with 0.4 threshold and 0.75-mm margin.

3.4. *In vivo BLT-guided treatment planning*

The PTV_{BLT} depicted in Fig. 7(d1-3) were used to demonstrate BLT-guided treatment planning. Two plans, 2 static (Fig. 8(a1-3)) and 12 hybrid beams (Fig. 8(b1-3)), were used to illustrate a high throughput less conformal vs. low throughput high conformal scenario, respectively. The detail of beam arrangement can be found in supplementary material Sec. 5, Table S1 and Fig. S2. For both plans, a 5×5 mm^2 beam collimator was used for each beam, and the CoM of GTV_{BLT} was set as the beam isocenter. A single dose of 5 Gy was prescribed to cover 95% of the PTV_{BLT} for each plan. The corresponding dose distributions for the 2-beam and 12-hybrid-beam plan are shown in Fig. 8(a1-3) and 8(b1-3), respectively. The GTV is covered by the dose volume of 5 Gy for both plans, indicating that a plan even as simple as the arrangement of 2 beams can effectively treat the tumor under BLT guidance. However, due to the simplicity of irradiation geometry, the 2-beam plan unavoidably delivered a large volume of high dose to normal tissue. In contrast, the plan with 12 hybrid beams performed highly conformal dose coverage to the GTV.

The dose-volume histogram (DVH; Fig. 8(c)) shows that 99.3% and 99.7% of GTV were covered by the 5-Gy prescribed dose with 2-beam and 12-beam plans, respectively. It is worthwhile to note that the dosimetric coverage for target volume is limited by the available collimator size which restricted us from choosing optimal isodose line best covering the targets, and thus introducing large dosimetric distribution at high isodose (5-8 Gy) inside the PTV_{BLT} and GTV. We used conformity index to quantify the conformity of dosage to PTV_{BLT}. At the prescribed dose of 5 Gy, the conformity indices for the 2-beam and 12-hybrid-beam plan are 2.6 and 1.5, respectively. These values indicate the superior conformity of the 12-hybrid-beam plan to PTV_{BLT} than the 2-beam case, which is consistent with Fig. 8(a-b). As shown in Fig. 8(c), due to the high conformality of coverage to PTV_{BLT}, 3.2% of normal tissue was irradiated at 5 Gy with the 12-beam plan vs. 5.9% of that with the 2-beam arrangement. At a dose volume as low

Biomedical Optics EXPRESS

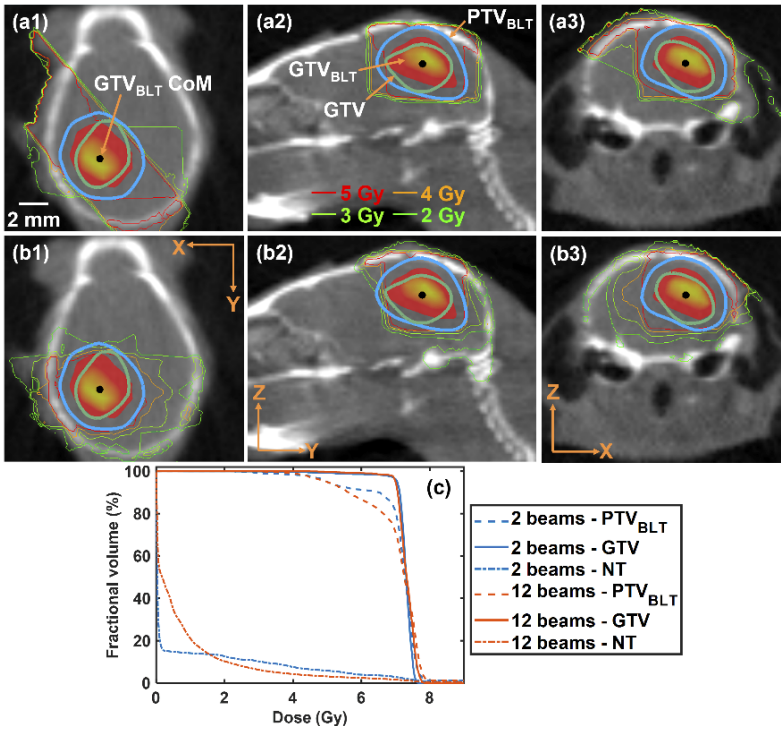

Fig. 8. Treatment plans of *in vivo* BLT-guided irradiation; The parameters of each beam for both plans are listed in Table S1. (a1-3) isodose distribution of a 2-beam plan; (b1-3) isodose distribution of a 12-hybrid (static + arc)-beam plan; for both plans, the visualization of beam arrangement is shown in Fig. S2. (c) Corresponding DVH of the 2-beam and 12-beam irradiations for PTV_{BLT}, GTV, and normal tissue (NT).

as 2 Gy, the 12-beam plan could still better alleviate normal tissue toxicity than the 2-beam plan (10.3% vs 12.7%). The 12-beam plan is expected to introduce larger portion of dose bath at < 1.5 Gy in normal tissue region, which is a trade-off for high conformality of target coverage and decrease of normal tissue inclusion at high dose.

4. Discussion

BLI offers high contrast and specificity to luciferase-labeled soft tissue targets with minimal background disturbance, and it has thus been applied for radiation guidance to pre-clinical cancer models [39,40]. However, intensity and distribution of BLI are nonlinearly correlated with internal source location, tissue optical properties, animal surface irregularity, and angle of view to animal surface [41,42], all of which impede the localization accuracy of BLI. Studies have revealed that a vertical beam guided through the strongest surface bioluminescence intensity could deviate from the CoM of an internal source by as much as 3.5 mm [39,43]. It renders one would need 3.5 mm radiation margin to ensure not missing target, which leads to large volumetric expansion and introduce normal tissue toxicity for small animal radiation study. Ultimately, it can be a detriment of experiment reproducibility. It is imperative for us to develop the 3D BLT for precise radiation guidance [24,29,41]. Compared to our previous study [24], establishing a systematic methodology and margin recipe of BLT for radiation guidance, the scope of current study focuses on technology innovations. Our innovations include multi-spectral and multi-projection optical system and thermostatic instrumentation, the design of mouse bed

Biomedical Optics EXPRESS

for optical system and radiation platform integration, and explicit co-registration to map 2D BLI onto 3D mesh surface generated from the CBCT imaging. This work has detailed our mobile BLT system and its capability to localize mouse phantom and *in vivo* target in 3D at < 1 mm accuracy and provided threshold and margin to delineate target volume for optimal radiation strategies.

We previously developed an on-board BLT-guided small animal irradiator system [41] that incorporated BLT and CBCT-guided irradiator into a unit to eliminate the animal transport between the optical system and irradiator. However, the on-board design would reduce the experimental throughput of both systems. Optical system is often used for longitudinal studies or tumor monitoring when irradiation guidance and 3D imaging are not needed. For the on-board design, when one uses the optical system, the small animal irradiator becomes unavailable for radiation studies. Small animal irradiators, e.g. SARRP in our institution, are commonly used as core equipment shared by many laboratories, so the availability and throughput are important for such highly-used equipment. In addition, the mechanical design of the on-board setting is SARRP-specific [41], making the difficulty of retrospectively fitting the optical system to older SARRP models or potentially utilizing the BLT system for other irradiators from different vendors. Given these considerations, we redesigned the BLT system as a mobile and standalone setting while ensure steady animal transportation between the optical and radiation systems to allow their best use. This setting has an advantage of parallel operation for both BLI/BLT and irradiation. Regarding the potential positioning error caused by animal transportation, based on our previous study [28], the positioning error can be maintained within 0.2 mm as long as the animals are anesthetized with effective immobilization during transportation and the BLT system is in close proximity (< 5 m) to the irradiator. Most importantly, when we mapped the 2D BLIs to the surface of 3D mesh generated from the CBCT image, this positioning error, if present, will be propagated to the data mapping, and finally to the BLT reconstruction, which had been accounted in our radiation margin.

Another key feature of our system is allowing animal positioned in nature lying position, compared to other optical systems with vertical configuration [44,45]. In addition to keep studied animals in comfort position, the lying configuration is consistent with the position required in commercial small animal irradiators [8]. The consistent positioning between the optical system and irradiator is important for precise irradiation guidance as well as for the adoption of our optical system by irradiator users. To maintain the animal position at nature lying position while effectively acquire the signals from imaged object at different projections, we innovated the 3-mirror system to rotate the focal plane around imaged object coaxially without moving the camera or object (Fig. 1). This design allows a compact system configuration, and simplify the mechanical requirement and long-term quality assurance in compared with the design of rotating optical camera [40].

One necessary development for our BLT-guided irradiation is the data registration between the 2D optical images and 3D CBCT image. The registration is critical as the CBCT imaging commonly adopted in commercial irradiators. The CBCT image is not only used to generate the mesh for finite element-based BLT reconstruction, but its coordinate is also used for radiation treatment planning. This work is not trivial as we must build a series of equations to describe the relationship between the 2D optical and 3D CBCT coordinate system, while we need to reach sub millimeter registration accuracy to achieve accurate reconstruction for irradiation guidance. Based upon the work by Cao *et al* [31], we utilized the pinhole camera model and calibration routine; the maximum deviation can be reached at < 0.6 mm and average registration accuracy can even be achieved < 0.3 mm (Fig. 5) for any given projection.

Due to the ill-posed nature of BLT, we employed the multi-spectral and multi-projection imaging acquisition to maximize the amount of measured data and reduce the instability of reconstruction [22,46–49]. In biological tissue, the propagation of bioluminescent photons is

Biomedical Optics EXPRESS

subject to spectral-dependent scattering and absorption, resulting in various extents of attenuation for these photons while propagating from source to object surface. Therefore, the source distribution in depth can be significantly improved by data measured at multiple wavelengths over that with single-wavelength input [22]. In our phantom study, compared to the 3-wavelength (610, 630, 650 nm) input, additional inclusion of data at 590 nm for the 4-wavelength input can improve the accuracy of BLT target localization (Fig. 6, b2-4 vs. b5-7). However, for the *in vivo* example, GBM model, due to the stronger tissue photon absorption, the bioluminescent signal at 590 nm was much weaker compared to that at other wavelengths. It in turn affected the stability of our spectral derivate-based BLT reconstruction, and was not chosen for the reconstruction. In sum, the multi-spectral image can improve tomographic reconstruction, but the choice of wavelength depends on underlying *in vivo* environment. The advantage of multi-projection setting is clearly shown in Fig. 6. Because the actual tumor location is usually unknown, the multi-projection setting provides user the option of where to image and how many projections used for reconstruction. Especially for abdominal site, such as pancreatic tumor, we have demonstrated in our previous work [50] that abdominal tumor can easily move to different location. It renders that 3D BLT with multiple-projection is needed to accurately quantify tumor location, particularly to guide irradiation for precise radiation research.

The extent of BLT-reconstructed volume, GTV_{BLT}, depends on the choice of volume threshold, ultimately determining the fidelity of volume delineation to actual tumor. There are various threshold values used in optical tomography studies [51–53]. Instead of using an empirical threshold for BLT-reconstructed volume, we employed the Dice coefficient to determine an optimal value. However, the accuracy of target positioning and delineation is inevitably hindered by the multiple scattering nature of tissue optics, underdetermined inverse problem in source reconstruction, and uncertainties of optical property determination, resulting in the challenge of precise recovery for the actual tumor location and shape *in vivo* by optical tomography. These are the long-existing hurdles for investigators applying optical tomography for *in vivo* use. We innovated the margin concept for optical tomography [24]. Despite the good target localization accuracy, 0.36 mm CoM deviation, being achieved, the remaining uncertainties in volume delineation can be further accounted by adding margin to GTV_{BLT} and expanding it to PTV_{BLT} (Fig. 7). This margin is a system-, i.e. instrument and reconstruction algorithm, specific parameter, including the target positioning and volume delineation uncertainties caused by our BLT-guided platform. Additional uncertainty such as radiation delivery error can be further added into margin expansion depending on the irradiator in use. In this study, we exploited the involvement of PTV_{BLT} in tumor and normal tissue. For the *in vivo* GBM mouse, 18 days after cell implanted, the PTV_{BLT} with 0.4 threshold and 0.75-mm margin provides 100% tumor coverage and 1.8% normal tissue involvement. However, the method of assessing actual tumor volume, such as the contrast-labelled CBCT imaging used in this study, is not always available for evaluating the optimal threshold value and margin. The 0.5 threshold was published previously [24] for a cohort of 10 mice for approximately 14-day-old GBM tumors. When the optimal threshold is not available, one can still apply the published value for specific tumor model, but add conservative margin to ensure tumor coverage with the trade-off against normal tissue toxicity.

The margin is critical to enable BLT-guided irradiation by reducing the variation of target coverage and providing a practical volume for radiation planning to allow conformal RT (Fig. 8). We now can explore the planning strategy similar to radiation oncology clinic setting. The high throughput less conformal 2-beam plan and the low throughput high conformal 12-beam plan were investigated. Because of less complexity of beam positioning, the 2-beam arrangement offered a straightforward solution for BLT-guided radiation delivery, which can be more efficient for high-throughput small animal RT in routine radiobiological studies. In the occasion where organ at risk is near target, the high conformal design could be needed to ensure experiment

Biomedical Optics EXPRESS

reproducibility. Researchers can employ an irradiation beam arrangement that best fits their radiation study by utilizing BLT volumetric guidance.

5. Conclusion

We have developed a novel BLT-guided system readily compatible with commercial small animal irradiator to provide focal irradiation guidance. We also explicated the procedures of applying BLT guidance for radiation planning to the *in vivo* orthotopic tumor model. Under proper justification on the reconstructed volume threshold and radiation margin establishment, our BLT platform can offer an attractive option of high contrast optical-image-guided irradiation for researchers in radiobiology to mimic clinical RT for orthotopic and spontaneous models. We expect the BLT-guided system enabling conformal irradiation for soft tissue targets, reducing normal tissue involvement and thus facilitating experimental reproducibility.

Funding. Xstrahl Ltd; Cancer Prevention and Research Institute of Texas (RR200042); National Cancer Institute (P30CA006973, R01CA240811, R21CA223403, R37CA230341).

Acknowledgments. We thank Dr. Michael Lim (Department of Neurosurgery, Stanford University, Palo Alto, California) for providing GL261-*Luc*2 cell line.

Disclosures. Dr. Iulian Iordachita receives royalties from Xstrahl Ltd (R).

Data Availability. Data underlying the results presented in this paper are not publicly available at this time but may be obtained from the authors upon request.

Supplemental document. See Supplement 1 for supporting content.

References

1. C. Nutting, D. P. Dearnaley, and S. Webb, "Intensity modulated radiation therapy: A clinical review," Br. J. Radiol. **73**(869), 459–469 (2000).
2. G. N. Marta, V. Silva, H. D. Carvalho, F. F. de Arruda, S. A. Hanna, R. Gadia, J. L. F. da Silva, S. F. M. Correa, C. Abreu, and R. Riera, "Intensity-modulated radiation therapy for head and neck cancer: Systematic review and meta-analysis," Radiother. Oncol. **110**(1), 9–15 (2014).
3. T. R. Mackie, J. Kapatoes, K. Ruchala, W. G. Lu, C. Wu, G. Olivera, L. Forrest, W. Tome, J. Welsh, R. Jeraj, P. Harari, P. Reckwerdt, B. Paliwal, M. Ritter, H. Keller, J. Fowler, and M. Mehta, "Image guidance for precise conformal radiotherapy," Int. J. Radiat. Oncol. Biol. Phys. **56**(1), 89–105 (2003).
4. L. Xing, B. Thorndyke, E. Schreibmann, Y. Yang, T. F. Li, G. Y. Kim, G. Luxton, and A. Koong, "Overview of image-guided radiation therapy," Med. Dosim. **31**(2), 91–112 (2006).
5. J. Wong, E. Armour, P. Kazanzides, U. Iordachita, E. Tryggestad, H. Deng, M. Matinfar, C. Kennedy, Z. J. Liu, T. Chan, O. Gray, F. Verhaegen, T. McNutt, E. Ford, and T. L. DeWeese, "High-resolution, small animal radiation research platform with X-ray tomographic guidance capabilities," Int. J. Radiat. Oncol. Biol. Phys. **71**(5), 1591–1599 (2008).
6. R. Clarkson, P. E. Lindsay, S. Ansell, G. Wilson, S. Jelveh, R. P. Hill, and D. A. Jaffray, "Characterization of image quality and image-guidance performance of a preclinical microirradiator," Med. Phys. **38**(2), 845–856 (2011).
7. R. Pidikiti, S. Stojadinovic, M. Speiser, K. H. Song, F. Hager, D. Saha, and T. D. Solberg, "Dosimetric characterization of an image-guided stereotactic small animal irradiator," Phys. Med. Biol. **56**(8), 2585–2599 (2011).
8. F. Verhaegen, P. Granton, and E. Tryggestad, "Small animal radiotherapy research platforms," Phys. Med. Biol. **56**(12), R55–R83 (2011).
9. E. E. Graves, H. Zhou, R. Chatterjee, P. J. Keall, S. S. Gambhir, C. H. Contag, and A. L. Boyer, "Design and evaluation of a variable aperture collimator for conformal radiotherapy of small animals using a microct scanner," Med. Phys. **34**(11), 4359–4367 (2007).
10. H. Sha, T. S. Udayakumar, P. B. Johnson, N. Dogan, A. Pollack, and Y. D. Yang, "An image guided small animal stereotactic radiotherapy system," Oncotarget **7**(14), 18825–18836 (2016).
11. G. S. Herter-Sprie, H. Korideck, C. L. Christensen, J. M. Herter, K. Rhee, R. I. Berbeco, D. G. Bennett, E. A. Akbay, D. Kozono, R. H. Mak, G. M. Makrigiorgos, A. C. Kimmelman, and K. K. Wong, "Image-guided radiotherapy platform using single nodule conditional lung cancer mouse models," Nat. Commun. **5**(1), 5870 (2014).
12. L. Seifert, G. Werba, S. Tiwari, N. N. G. Ly, S. Nguy, S. Alothman, D. Alqunaibit, A. Avanzi, D. Daley, R. Barilla, D. Tippens, A. Torres-Hernandez, M. Hundeyin, V. R. Mani, C. Hajdu, I. Pellicciotta, P. Oh, K. Du, and G. Miller, "Radiation therapy induces macrophages to suppress t-cell responses against pancreatic tumors in mice," Gastroenterology **150**(7), 1659–1672.e5 (2016).
13. A. Chandra, T. Lin, M. B. Tribble, J. Zhu, A. R. Altman, W. J. Tseng, Y. J. Zhang, S. O. Akintoye, K. Cengel, X. S. Liu, and L. Qin, "Pth1-34 alleviates radiotherapy-induced local bone loss by improving osteoblast and osteocyte survival," Bone **67**, 33–40 (2014).

Biomedical Optics EXPRESS

14. C. Vanhove and I. Goethals, "Magnetic resonance imaging-guided radiation therapy using animal models of glioblastoma," Br J Radiol **92**(1095), 20180713 (2019).
15. E. Mikhaylova, J. Brooks, D. M. Zuro, F. Nouizi, M. Kujawski, S. S. Madabushi, J. Y. Qi, M. X. Zhang, J. Chea, E. K. Poku, N. Bowles, J. Y. C. Wong, J. E. Shively, P. J. Yazaki, G. Gulsen, S. R. Cherry, and S. K. Hui, "Prototype small-animal PET-CT imaging system for image-guided radiation therapy," IEEE Access **7**, 143207–143216 (2019).
16. S. H. Thorne and C. H. Contag, "Using in vivo bioluminescence imaging to shed light on cancer biology," Proc. IEEE **93**(4), 750–762 (2005).
17. K. O'Neill, S. K. Lyons, W. M. Gallagher, K. M. Curran, and A. T. Byrne, "Bioluminescent imaging: A critical tool in pre-clinical oncology research," J. Pathol. **220**(3), 317–327 (2010).
18. D. M. Close, T. T. Xu, G. S. Sayler, and S. Ripp, "In vivo bioluminescent imaging (BLI): Noninvasive visualization and interrogation of biological processes in living animals," Sensors **11**(1), 180–206 (2010).
19. D. E. Jenkins, Y. Oei, Y. S. Hornig, S. F. Yu, J. Dusich, T. Purchio, and P. R. Contag, "Bioluminescent imaging (BLI) to improve and refine traditional murine models of tumor growth and metastasis," Clin. Exp. Metastasis **20**(8), 733–744 (2003).
20. J. J. Yu, B. Zhang, I. I. Iordachita, J. Reyes, Z. H. Lu, M. V. Brock, M. S. Patterson, J. W. Wong, and K. K.-H. Wang, "Systematic study of target localization for bioluminescence tomography guided radiation therapy," Med. Phys. **43**(5), 2619–2629 (2016).
21. G. Wang, W. X. Cong, K. Durairaj, X. Qian, H. Shen, P. Sinn, E. Hoffman, G. McLennan, and M. Henry, "In vivo mouse studies with bioluminescence tomography," Opt. Express **14**(17), 7801–7809 (2006).
22. C. Kuo, O. Coquoz, T. L. Troy, H. Xu, and B. W. Rice, "Three-dimensional reconstruction of in vivo bioluminescent sources based on multispectral imaging," J. Biomed. Opt. **12**(2), 024007 (2007).
23. V. Ntziachristos, J. Ripoll, L. V. Wang, and R. Weissleder, "Looking and listening to light: The evolution of whole-body photonic imaging," Nat. Biotechnol. **23**(3), 313–320 (2005).
24. X. Xu, Z. Deng, H. Dehghani, I. Iordachita, M. Lim, J. W. Wong, and K. K.-H. Wang, "Quantitative bioluminescence tomography-guided conformal irradiation for preclinical radiation research," Int. J. Radiat. Oncol. Biol. Phys. **111**(5), 1310–1321 (2021).
25. J. A. Guggenheim, H. Dehghani, H. Basevi, I. B. Styles, and J. Frampton, "Development of a multi-view, multi-spectral bioluminescence tomography small animal imaging system," in *Diffuse optical imaging III*, A. H. Hielscher and P. Taroni, eds. (Spie-Int Soc Optical Engineering, 2011), Vol. 8088.
26. H. Dehghani, J. A. Guggenheim, S. L. Taylor, X. K. Xu, and K. K.-H. Wang, "Quantitative bioluminescence tomography using spectral derivative data," Biomed. Opt. Express **9**(9), 4163–4174 (2018).
27. K. Ogoh, R. Akiyoshi, T. May Maw, T. Sugiyama, S. Dosaka, Y. Hatta-Ohashi, and H. Suzuki, "Bioluminescence microscopy using a short focal-length imaging lens," J. Microsc. **253**(3), 191–197 (2014).
28. B. Zhang, J. W. Wong, I. I. Iordachita, J. Reyes, K. Nugent, P. T. Tran, S. W. Tuttle, C. Koumenis, and K. K.-H. Wang, "Evaluation of on- and off-line bioluminescence tomography system for focal irradiation guidance," Radiat. Res. **186**(6), 592–601 (2016).
29. Z. Deng, X. Xu, T. Garzon-Muvdi, Y. Xia, E. Kim, Z. Belcaid, A. Luksik, R. Maxwell, J. Choi, H. Wang, J. Yu, I. Iordachita, M. Lim, J. W. Wong, and K. K.-H. Wang, "In vivo bioluminescence tomography center of mass-guided conformal irradiation," Int. J. Radiat. Oncol. Biol. Phys. **106**(3), 612–620 (2020).
30. Y. D. Yang, K. K.-H. Wang, S. Eslami, I. I. Iordachita, M. S. Patterson, and J. W. Wong, "Systematic calibration of an integrated X-ray and optical tomography system for preclinical radiation research," Med. Phys. **42**(4), 1710–1720 (2015).
31. L. Cao, M. Breithaupt, and J. Peter, "Geometrical co-calibration of a tomographic optical system with CT for intrinsically co-registered imaging," Phys. Med. Biol. **55**(6), 1591–1606 (2010).
32. M. Schweiger, S. R. Arridge, M. Hiraoka, and D. T. Delpy, "The finite-element method for the propagation of light in scattering media - boundary and source conditions," Med. Phys. **22**(11), 1779–1792 (1995).
33. H. Dehghani, M. E. Eames, P. K. Yalavarthy, S. C. Davis, S. Srinivasan, C. M. Carpenter, B. W. Pogue, and K. D. Paulsen, "Near infrared optical tomography using NIRFAST: Algorithm for numerical model and image reconstruction," Commun. Numer. Methods Eng. **25**(6), 711–732 (2009).
34. H. R. A. Basevi, K. M. Tichauer, F. Leblond, H. Dehghani, J. A. Guggenheim, R. W. Holt, and I. B. Styles, "Compressive sensing based reconstruction in bioluminescence tomography improves image resolution and robustness to noise," Biomed. Opt. Express **3**(9), 2131–2141 (2012).
35. A. J. Lin, M. A. Koike, K. N. Green, J. G. Kim, A. Mazhar, T. B. Rice, F. M. LaFerla, and B. J. Tromberg, "Spatial frequency domain imaging of intrinsic optical property contrast in a mouse model of Alzheimer's disease," Ann. Biomed. Eng. **39**(4), 1349–1357 (2011).
36. R. Kikinis, S. D. Pieper, and K. G. Vosburgh, "3D slicer: A platform for subject-specific image analysis, visualization, and clinical support," in *Intraoperative imaging and image-guided therapy*, F. A. Jolesz, ed. (Springer New York, New York, NY, 2014), pp. 277–289.
37. A. Fedorov, R. Beichel, J. Kalpathy-Cramer, J. Finet, J. C. Fillion-Robin, S. Pujol, C. Bauer, D. Jennings, F. Fennessy, M. Sonka, J. Buatti, S. Aylward, J. V. Miller, S. Pieper, and R. Kikinis, "3D slicer as an image computing platform for the quantitative imaging network," Magn. Reson. Imaging **30**(9), 1323–1341 (2012).
38. L. Feuvret, G. Noël, J.-J. Mazeron, and P. Bey, "Conformity index: A review," Int. J. Radiat. Oncol. Biol. Phys. **64**(2), 333–342 (2006).

Biomedical Optics EXPRESS

39. R. Tuli, A. Surmak, J. Reyes, A. Hacker-Prietz, M. Armour, A. Leubner, A. Blackford, E. Tryggestad, E. M. Jaffee, J. Wong, T. L. DeWeese, and J. M. Herman, "Development of a novel preclinical pancreatic cancer research model: Bioluminescence image-guided focal irradiation and tumor monitoring of orthotopic xenografts," Transl. Oncol. **5**(2), 77–84 (2012).
40. R. A. Weersink, S. Ansell, A. Wang, G. Wilson, D. Shah, P. E. Lindsay, and D. A. Jaffray, "Integration of optical imaging with a small animal irradiator," Med. Phys. **41**(10), 102701 (2014).
41. B. Zhang, K. K.-H. Wang, J. J. Yu, S. Eslami, I. Iordachita, J. Reyes, R. Malek, P. T. Tran, M. S. Patterson, and J. W. Wong, "Bioluminescence tomography-guided radiation therapy for preclinical research," Int. J. Radiat. Oncol. Biol. Phys. **94**(5), 1144–1153 (2016).
42. A. D. Klose and N. Paragas, "Automated quantification of bioluminescence images," Nat. Commun. **9**(1), 4262 (2018).
43. R. Tuli, M. Armour, A. Surmak, J. Reyes, I. Iordachita, M. Patterson, and J. Wong, "Accuracy of off-line bioluminescence imaging to localize targets in preclinical radiation research," Radiat. Res. **179**(4), 416–421 (2013).
44. N. Deliolanis, T. Lasser, D. Hyde, A. Soubret, J. Ripoll, and V. Ntziachristos, "Free-space fluorescence molecular tomography utilizing 360° geometry projections," Opt. Lett. **32**(4), 382–384 (2007).
45. J. Shi, K. Xu, A. Keyvanloo, T. S. Udayakumar, A. Ahmad, F. Yang, and Y. Yang, "A multimodality image guided precision radiation research platform: Integrating X-ray, bioluminescence, and fluorescence tomography with radiation therapy," Int. J. Radiat. Oncol. Biol. Phys. **108**(4), 1063–1072 (2020).
46. A. X. Cong and G. Wang, "Multispectral bioluminescence tomography: Methodology and simulation," Int. J. Biomed. Imaging **2006**, 1–7 (2006).
47. H. Dehghani, S. C. Davis, S. D. Jiang, B. W. Pogue, K. D. Paulsen, and M. S. Patterson, "Spectrally resolved bioluminescence optical tomography," Opt. Lett. **31**(3), 365–367 (2006).
48. A. D. Klose and T. Poschinger, "Excitation-resolved fluorescence tomography with simplified spherical harmonics equations," Phys. Med. Biol. **56**(5), 1443–1469 (2011).
49. M. A. Lewis, E. Richer, N. V. Slavine, V. D. Kodibagkar, T. C. Soesbe, P. P. Antich, and R. P. Mason, "A multi-camera system for bioluminescence tomography in preclinical oncology research," Diagnostics **3**(3), 325–343 (2013).
50. Z. Deng, X. Xu, H. Dehghani, J. Reyes, L. Zheng, A. Klose, J. Wong, P. Tran, and K. K.-H. Wang, "In vivo bioluminescence tomography-guided radiation research platform for pancreatic cancer: An initial study using subcutaneous and orthotopic pancreatic tumor models," Proc. SPIE **11224**, 9 (2020).
51. Y. Zilberman, I. Kallai, Y. Gafni, G. Pelled, S. Kossodo, W. Yared, and D. Gazit, "Fluorescence molecular tomography enables in vivo visualization and quantification of nonunion fracture repair induced by genetically engineered mesenchymal stem cells," J. Orthop. Res. **26**(4), 522–530 (2008).
52. V. Ntziachristos, E. A. Schellenberger, J. Ripoll, D. Yessayan, E. Graves, A. Bogdanov, L. Josephson, and R. Weissleder, "Visualization of antitumor treatment by means of fluorescence molecular tomography with an annexin v–cy5.5 conjugate," Proc. Natl. Acad. Sci. USA **101**(33), 12294–12299 (2004).
53. G. Zacharakis, H. Kambara, H. Shih, J. Ripoll, J. Grimm, Y. Saeki, R. Weissleder, and V. Ntziachristos, "Volumetric tomography of fluorescent proteins through small animals in vivo," Proc. Natl. Acad. Sci. USA **102**(51), 18252–18257 (2005).